Published in final edited form as:
J Appl Biomech. 2014 June ; 30(3): 461–470. doi:10.1123/jab.2013-0112.

Accuracy and Feasibility of Dual Fluoroscopy and Model-Based Tracking to Quantify *In Vivo* Hip Kinematics During Clinical Exams

Ashley L. Kapron[1,2], **Stephen K. Aoki**[1], **Christopher L. Peters**[1], **Steve A. Maas**[2,3], **Michael J. Bey**[4], **Roger Zauel**[4], and **Andrew E. Anderson**[1,2,3,5]

[1]Department of Orthopaedics, University of Utah, Salt Lake City, UT, United States

[2]Department of Bioengineering, University of Utah, Salt Lake City, UT, United States

[3]Scientific Computing and Imaging Institute, University of Utah, Salt Lake City, UT, United States

[4]Bone and Joint Center, Department of Orthopaedics, Henry Ford Hospital, Detroit, MI, United States

[5]Department of Physical Therapy, University of Utah, Salt Lake City, UT, United States

Abstract

Accurate measurements of in-vivo hip kinematics may elucidate the mechanisms responsible for impaired function and chondrolabral damage in hips with femoroacetabular impingement (FAI). The objectives of this study were to quantify the accuracy and demonstrate the feasibility of using dual fluoroscopy to measure in-vivo hip kinematics during clinical exams used in the assessment of FAI. Steel beads were implanted into the pelvis and femur of two cadavers. Specimens were imaged under dual fluoroscopy during the impingement exam, FABER test, and rotational profile. Bead locations measured with model-based tracking were compared to those measured using dynamic radiostereometric analysis. Error was quantified by bias and precision, defined as the average and standard deviation of the differences between tracking methods, respectively. A normal male volunteer was also imaged during clinical exams. Bias and precision along a single axis did not exceed 0.17 and 0.21 mm, respectively. Comparing kinematics, positional error was less than 0.48 mm and rotational error was less than 0.58°. For the volunteer, kinematics were reported as joint angles and bone-bone distance. These results demonstrate that dual fluoroscopy and model-based tracking can accurately measure hip kinematics in living subjects during clinical exams of the hip.

Corresponding Address: Andrew E. Anderson, PhD, University of Utah, Department of Orthopaedics, 590 Wakara Way, Rm A100, Salt Lake City, UT 84102, Phone: 801.587.5208, Fax: 801.587.5211, Andrew.Anderson@hsc.utah.edu.

Conflict of Interest Disclosure: None of the authors have conflicts of interest with the research herein.

To view the four supplemental videos, please use click here, which should lead to this Web address: http://videos.humankinetics.com/services/player/bcpid3172241376001?bckey=AQ~~,AAAA0gHQG-E~,UzAFL1pLzn6s_0oR7iutk5BQCzT-zy6W

Keywords

clinical biomechanics; femoroacetabular impingement; motion analysis; musculoskeletal; orthopaedics

Introduction

Chondrolabral damage in hips with femoroacetabular impingement (FAI) may result from motion conflict due to acetabular overcoverage, femoral head asphericity, or both. Three physical exams are used to evaluate FAI patients: 1) internal/external rotational profile, 2) impingement exam, and 3) flexion-abduction-external rotation (FABER) test.[1] These clinical exams place the hip into the limits of motion to initiate impingement. Range of motion during the exams is then quantified with a goniometer or estimated visually. However, without accurate measurements of hip kinematics for those motions believed to induce impingement, it remains unknown how, exactly, the altered anatomy in patients with FAI causes motion conflict. A more accurate methodology to measure and visualize hip kinematics in a research setting could confirm or refute the hypothesized mechanism of impingement, and provide data that could improve the diagnosis and treatment of FAI.

Researchers have employed skin marker motion analysis,[2–4] computer simulations,[5–8], dynamic CT[9] and single plane fluoroscopy[10] in the study of FAI. However, skin marker motion analysis assumes joint centers and axes, and markers are subject to substantial motion artifact. Computer simulations assume kinematics and neglect bulk soft tissue restraints. Dynamic CT exhibits motion blur, and single plane fluoroscopy has poor out-of-plane accuracy.

Dual radiography and model-based tracking software could accurately quantify hip kinematics without the limitations of the aforementioned techniques.[11] However, previous applications of dual radiography to the native hip have investigated motions occurring primarily in the sagittal plane (walking, rising from a chair).[12,13] Quantifying motion during clinical exams that incorporate hip rotation and ab/adduction at extreme ranges of motion may be more applicable to the study of FAI. The objectives of this study were to: 1) quantify the accuracy and, 2) demonstrate the feasibility of using dual fluoroscopy to measure in-vivo hip kinematics during clinical exams used in the assessment of FAI.

Methods

Dual Fluoroscopy System (DFS)

A custom DFS (Radiological Imaging Services, Hamburg, PA) was developed, which consisted of two x-ray emitters (Housing B-100/Tube A-142, Varian, Salt Lake City, UT) and two 12” image intensifiers (T12964-P/S, Dunlee Inc., Aurora, IL), each mounted to a dedicated base. The DFS was positioned around a radiolucent table to image hips supine (Figure 1). The fluoroscopy configuration was determined in preliminary cadaveric testing. The configuration enabled the clinician and subject to complete the exam without contact to the system, and minimized bone and soft tissue overlap in the images during all three exams. The source to II distances of fluoroscopes 1 and 2 were 1100 and 1145 mm, respectively.

The interbeam angle was 46° and the approximate imaging volume was 8500 cm^3 (sufficient to capture the proximal femur and the majority of the hemipelvis of interest, Figure 2).

All images in this study were acquired during continuous fluoroscopy using high speed digital cameras (Phantom Miro 3, Vision Research, Wayne, NJ) at 100 Hz with 608×600 resolution and 3000 μs camera exposure. Images of a grid of steel beads corrected distortion.[14] An acrylic calibration frame housing 36 steel beads (3 mm diameter, spacing 6.35 cm, uncertainty 0.0036 mm) was used to define the position and orientation of the DFS in a laboratory coordinate system.

Validation of Dynamic Radiostereometric Analysis (DRSA): Optimal Conditions

This study represented the first use of the described dual fluoroscopy system. Thus, a simple test was performed to quantify the accuracy of dynamic radiostereometric analysis (DRSA) under optimal conditions. An acrylic plate with steel beads spaced 30 mm (2 mm diameter, positional uncertainty 0.0013 mm) was imaged during random motion.[15] 3D positions of the beads in laboratory coordinates were calculated using direct linear transform theory.[15] Tracked bead inter-centroid distances were compared to known distances to quantify accuracy. Bias and precision was defined by the average and standard deviation of the differences for 400 frames, respectively.

Validation of Model-Based Tracking

Two pelvis-toe cadaveric specimens were acquired (Specimen 1: male, 57 years old, 170 cm, 70 kg, BMI 24.2; Specimen 2: female, 59 years old, 168 cm, 50 kg, BMI 17.7). Steel beads (2 mm diameter) were implanted into the left hemipelvis and femur with a minimally invasive approach preserving all soft tissue (Figure 2). At least five beads were implanted into each bone. Bead locations were chosen so as to minimize disruption of soft tissue. Incisions were closed with suture. CT images of the entire pelvis, proximal femurs, and knees were acquired with a Siemens Somatom CT Scanner (0.7 mm slice thickness, Specimen 1/Specimen 2: 405/424 mm FOV, 512×512 matrix). Data were upsampled to 3× resolution to reduce stair-case artifact.[16] Bones were segmented semi-automatically using Amira (5.4.1, Visage Imaging, San Diego, CA). Pixels representing the implanted beads were automatically segmented and fit to a sphere to define bead centroids in CT coordinates.

The pelvis was secured to the radiolucent table with Velcro straps. Fluoroscopy video was acquired for the impingement exam (Supplemental Video 1; please see the last page of this PDF for captions that describe the videos), FABER test, and supine straight-legged int/external rotational profile. Three trials were collected per exam. Specimen 1 was imaged at 83 kVp/3.1 mA (fluoro 1) and 85 kVp/3.2 mA (fluoro 2). Specimen 2 was imaged at 73 kVp/2.9 mA (fluoro 1) and 74 kVp/2.5 mA (fluoro 2). The total number of frames for each exam was 331 ± 60.7 (average, standard deviation).

Using 3D bone reconstructions from the CT data, a pair of digitally reconstructed radiographs (DRRs) was generated using model-based tracking software.[11] CT pixels representing the beads and associated metal artifact (that was confined to immediate region of the bead only) were assigned intensities of surrounding bone. The position and orientation of the bones were calculated by optimizing agreement between the two DRRs and the

fluoroscope images.[11] With the position of each bone and the relative location of each bead centroid known, the Cartesian coordinates of each bead centroid in laboratory coordinates were calculated for each video frame. A custom PC with four GPUs (Tesla C1060, Nvidia, Santa Clara, CA) completed the optimization for each frame in 0.1–1.0 s.

DRSA of the implanted beads served as the reference standard. There were a few frames in each exam for which all five beads were not clearly visible. Thus, the three most visible beads in each bone for each trial were tracked. Standard deviations of the inter-bead distances defined the *in vitro* precision of DRSA. Precision results were averaged across trials. For comparison to model-based tracking, the coordinates of the beads relative to the laboratory system were smoothed with a 4th-order lowpass Butterworth filter with a cutoff frequency of 6 Hz.[17] Model-based tracking and filtered DRSA bead locations were compared for each trial. Bias and precision of the Euclidian distance between bead locations and the distance along each of the laboratory axes were calculated. Results were averaged across trials and specimens.

Anatomical Coordinate System Definition

Anatomical coordinate systems for the pelvis and femur were defined according to Wu et al.[18] Bony landmarks were selected automatically or semi-automatically using PreView and PostView (Musculoskeletal Research Laboratories, University of Utah, Salt Lake City, UT). Specifically, principal curvature automatically defined the lunate surface of the acetabulum, iliac crest and superior border of the sacroiliac joint on the pelvis and the femoral head, articulating surface of the femoral condyles, and ridges on the medial and lateral femoral epicondyles. The pelvic and femoral joint centers (PJC_{CT}, FJC_{CT}) were calculated as the center of the best fit sphere of the lunate surface of the acetabulum and femoral head, respectively (Figure 3). For the medial-lateral axis of the femur and midpoint of the knee, a plane was fit to the medial and lateral epicondyle ridges to isolate the posterior region of the condyles, which was then automatically fit to a cylinder (Figure 4). The center of the cylinder defined the midpoint of the knee.

The posterior superior iliac spine (PSIS) was defined as the posterior intersection of the superior border of the sacroiliac joint and the medial border of the iliac crest (Figure 5). The anterior superior iliac spine (ASIS) was defined as the anterior intersection between the medial and lateral borders of the iliac crest (Figure 5). While each of these of these borders was defined automatically by curvature, there was a small region of nodes at their intersections, of which the user selected a single node to represent the landmark. As the process was not fully automatic, a repeatability study was completed for the ASIS and PSIS. Specifically, three observers selected the landmarks three times to calculate inter- and intra-observer precision following the definition used by Victor et al.[19] The average position of each landmark across all nine selection trials was used in subsequent analyses. To evaluate the influence of landmark selection inconstancies, the pelvic coordinate system was calculated using the average landmark positions and the positions from each selection trial. For each axis of the coordinate system, the angle between the average and trial configurations was calculated.

Validation of Joint Angles and Translations

Raw model-based tracking and DRSA results were converted into clinical joint angles and translations. The transformation matrix relating the pelvis and femur anatomical coordinate systems to the CT coordinate system (P_{anat}/CT and F_{anat}/CT) was defined using the landmarks described above. Not all bony landmarks required to define the anatomical coordinate systems were visible in the dual fluoroscopy field of view. As such, a technical coordinate system was required for both the pelvis and femur, and established relative to the CT coordinate system using the three most visible beads (P_{tech}/CT and F_{tech}/CT). These technical coordinate systems were then tracked relative to laboratory coordinates (P_{tech}/Lab and F_{tech}/Lab) for each fluoroscopy frame for both model-based tracking and DRSA. The combination of these matrices provided the overall transformation from pelvis to femur anatomical coordinate systems for each frame, calculated as:

$$P_{anat}/CT \times CT/P_{tech} \times P_{tech}/Lab \times Lab/F_{tech} \times F_{tech}/CT \times CT/F_{anat}.$$

The three joint angles (flexion/extension, abduction/adduction, internal/external rotation) were calculated from the resulting transformation matrix using a Grood and Suntay convention.[20]

To define translations, the position of the PJC and FJC was calculated in laboratory coordinates for each frame as follows (example for the PJC):

$$PJC_{Lab}=Lab/P_{tech} \times P_{tech}/CT \times PJC_{CT}.$$

The vector from PJC to FJC was computed and then projected onto each of the pelvic coordinate axes (also recalculated for the current frame) to obtain medial/lateral, anterior/posterior, superior/inferior translations. Joint angles and translations derived from raw DRSA bead coordinates were filtered with a 6 Hz Butterworth filter. Bias and precision were calculated between the filtered DRSA kinematics and raw model-based tracking kinematics.

Repeatability of the clinical exams was assessed at max external rotation (FABER), max internal rotation (Rotational Profile) and max internal rotation in flexion (for the Impingement Exam). Each time point was identified in the trial and the three joint angles were recorded. Exam repeatability was calculated as the standard deviation of each angle over the three trials.

Validation of Bone-Bone Distance

A custom tool was created in PostView (Musculoskeletal Research Laboratories, University of Utah, Salt Lake City, UT) to visualize bone motion and bone-bone distance. For bone motion, the tool applied transformations from CT to laboratory coordinates for both the femur and pelvis for each time point to nodal coordinates defining the bone surfaces. For bone-bone distance, the user selected the faces representing the articulating regions of the acetabulum and femur. For each face, the tool calculated the nearest distance to the opposing surface (displayed as a fringe plot).

Bone-bone distance results were compared between DRSA and model-based tracking. For every 10^{th} frame of each exam, the root mean square (RMS) error was calculated between

all nodes in the articulating region of the pelvis and femur (defined as nodes with a distance less than 10 mm measured by either tracking method). An average RMS error was calculated for each trial and then results were averaged across all specimens and exams.

Application to Live Human Subject

With IRB approval (#51053) and informed consent, one male with no history of hip pain or pathology was imaged (32 years old, 177 cm, 73 kg, BMI 23.3). An orthopaedic surgeon performed the three exams (Figure 6). 280 ± 5 frames were collected per exam. Radiation settings were 87 kVp/3.3 mA (fluoro 1) and 88 kVp/3.4 mA (fluoro 2). CT images of the entire pelvis, proximal femur, and knee were acquired with a Siemens SOMATOM Definition CT Scanner (0.7 mm slice thickness, 355 mm FOV, 512 × 512 matrix) and bones were segmented with Amira. Model-based tracking and filtering of results was completed as described above. Outcome measures included joint angles, translations, bone-bone distance, and videos of bone motion.

Results

Bias and precision of DRSA for the optimal conditions (beads in acrylic) were 0.017 and 0.113 mm, respectively. *In vitro* precision (± standard deviation across all trials and specimens) of DRSA was 0.159 ± 0.072 mm.

Average Euclidian bias of model-based tracking (± standard deviation across all trials and specimens) was 0.32 ± 0.08 mm for the pelvis and 0.30 ± 0.06 mm for the femur. Average Euclidian precision for the pelvis and femur were 0.13 ± 0.03 mm and 0.14 ± 0.04, respectively. Across exams, bias and precision of the distance difference along any one of the laboratory axes did not exceed 0.17 mm and 0.23 mm, respectively (Table 1).

For Specimen 1, Euclidian bias and precision across all trials were 0.35 ± 0.05 and 0.13 ± 0.02 for the pelvis, respectively, and 0.29 ± 0.04 mm and 0.13 ± 0.03 for the femur, respectively. For Specimen 2, the Euclidian bias and precision across all trials were 0.30 ± 0.11 and 0.13 ± 0.04 for the pelvis, respectively, and 0.31 ± 0.09 mm and 0.15 ± 0.05 for the femur, respectively.

Intra-observer precision in landmark selection (± standard deviation across all observer trials) for the ASIS and PSIS were 0.18 ± 0.44 mm and 0.12 ± 0.37 mm, respectively. Inter-observer precision was 0.18 ± 0.21 mm for the ASIS and 0.24 ± 0.38 mm for the PSIS. Comparing pelvic coordinate systems established using landmarks from each selection trial to the coordinate system established from the average position of each landmark, the average angle between respective axes was 0.07 ± 0.10°.

Comparing model-based tracking kinematics to DRSA kinematics, translation bias did not exceed 0.48 mm and angular bias did not exceed 0.58° (Table 2). Qualitatively, kinematics were nearly identical between DRSA and model-based tracking (visualized for the impingement exam on Specimen 1 in Figure 7). Exam repeatability ranged from 0.1° (for ab/adduction angle at the point of max internal rotation during the rotational profile) to 4.1° (for ab/adduction angle at the point of max external rotation during the FABER test). The

average RMS error of bone to bone measurements (± standard deviation across all trials and specimens) was 0.52 ± 0.15 mm.

The total time used to position the live subject and image all exams was 21 seconds, resulting in an estimated dose exposure (EDE) from dual fluoroscopy of 0.32 mSv. The EDE of the CT scan was 9.42 mSv. For the three exams, joint angles and bone to bone distance was displayed in the articulating region (Figure 8). Greater external rotation than internal rotation was achieved during the rotational profile. At maximum adduction during the impingement exam, the anterior femoral neck approximated the anterosuperior acetabular rim (shortest bone-bone distance was approximately 2 mm – Figure 8). For the FABER test, the femur achieved 65° of external rotation in the figure-four position.

Bone motion and dynamic bone to bone distance fringe plots for all three exams are included as supplemental videos (please see the last page of this PDF for captions that describe the videos). During the impingement exam, the pelvis remained relatively stationary until t=~1.25 sec, after which the force applied by the examiner caused posterior pelvic tilt and pelvic obliquity (Supplemental Video 2). During the FABER test, subtle subluxation occurred as the posterior femoral neck articulated against the posterior acetabular wall (Supplemental Video 3). For the rotational profile, internal rotation did not appear to be limited by articulation of the femoral head or neck with the acetabular rim (Supplemental Video 4).

Discussion

In this study, dual fluoroscopy and model-based tracking could measure hip kinematics during clinical exams to a bias and precision less than one millimeter and one degree, similar to other hip validation studies (Table 3). There were no substantial differences in tracking accuracy between exams. Exam repeatability for the cadavers was very good. The semi-automatic approach described for landmark selection had excellent repeatability; minor inconsistencies in landmark selection only slightly altered coordinate axes. A live subject was also successfully imaged. Joint angles, translations and bone-bone distance results as well as videos of bone motion for the volunteer demonstrated the feasibility of using dual radiography and model-based tracking for future research.

It should be noted that the bias and precision of model-based tracking presented herein represent the upper bounds of error. Specifically, bead locations quantified by DRSA served as the reference standard, but beads implanted in bone are more difficult to visualize than those in a radiolucent material, like acrylic. As a result, the precision of DRSA was slightly worse *in vitro* than in the optimal conditions. In the past, inaccuracies in *in vitro* DRSA have been addressed by excluding those image frames with poor DRSA precision.[13] By excluding frames, one may artificially improve accuracy of model-based tracking. Rather than excluding frames in the present study, we chose to filter the *in vitro* DRSA data. We chose to filter the experimental data and retain the raw model-based tracking data as we believe this represents a worst-case scenario.

There were a few limitations. First, while the study objective was to evaluate clinical exams utilized in the assessment of FAI, the live subject evaluated herein did not have FAI. However, normal subjects likely have a larger range of motion than FAI patients, which provides confidence that our DFS could quantify kinematics of FAI patients. The BMI of the cadaver specimens and volunteer were less than the United States average (28.7 kg/m^2).[21] However, Harris et al. reported a BMI of 24.5±2.6 kg/m^2 in a review of more than 2,000 FAI patients, making the results of this study relevant to the future study of FAI with dual-fluoroscopy and model-based tracking.[22] Still, the radiation and imaging settings used in our study may not be applicable to overweight or obese individuals. Nonetheless, use of ionizing radiation, especially with regards to CT, needs to be carefully evaluated. We chose to reduce radiation exposure to the human volunteer by performing a single trial. Therefore, a final limitation was that exam repeatability was accessed using the cadaveric specimens only.

In conclusion, by combining dual fluoroscopy with model-based tracking, we have shown that hip kinematics can be accurately quantified during clinical exams in-vivo. The ability to accurately quantify joint angles, visualize bone motion and distance between bones could provide insight into how FAI alters hip kinematics and elucidate the mechanisms responsible for chondrolabral damage.

Supplementary Material

Refer to Web version on PubMed Central for supplementary material.

Acknowledgments

Funding: University of Utah Seed Grant #51003326, University of Utah Department of Orthopaedics.

The authors acknowledge Kristin Ciarelli for assistance with model-based tracking.

References

1. Philippon MJ, Maxwell RB, Johnston TL, Schenker M, Briggs KK. Clinical presentation of femoroacetabular impingement. Knee Surg Sports Traumatol Arthrosc. 2007; 15(8):1041–1047. [PubMed: 17497126]
2. Kennedy MJ, Lamontagne M, Beaule PE. Femoroacetabular impingement alters hip and pelvic biomechanics during gait: Walking biomechanics of FAI. Gait Posture. 2009; 30(1):41–44. [PubMed: 19307121]
3. Rylander JH, Shu B, Andriacchi TP, Safran MR. Preoperative and postoperative sagittal plane hip kinematics in patients with femoroacetabular impingement during level walking. Am J Sports Med. 2011; 39(Suppl):36S–42S. [PubMed: 21709030]
4. Brisson N, Lamontagne M, Kennedy MJ, Beaule PE. The effects of cam femoroacetabular impingement corrective surgery on lower-extremity gait biomechanics. Gait Posture. 2013; 37(2): 258–263. [PubMed: 22939410]
5. Audenaert EA, Mahieu P, Pattyn C. Three-dimensional assessment of cam engagement in femoroacetabular impingement. Arthroscopy. 2011; 27(2):167–171. [PubMed: 20952150]
6. Tannast M, Kubiak-Langer M, Langlotz F, Puls M, Murphy SB, Siebenrock KA. Noninvasive three-dimensional assessment of femoroacetabular impingement. J Orthop Res. 2007; 25(1):122–131. [PubMed: 17054112]
7. Kubiak-Langer M, Tannast M, Murphy SB, Siebenrock KA, Langlotz F. Range of motion in anterior femoroacetabular impingement. Clin Orthop Relat Res. 2007; 458:117–124. [PubMed: 17206102]

8. Bedi A, Dolan M, Hetsroni I, et al. Surgical treatment of femoroacetabular impingement improves hip kinematics: a computer-assisted model. Am J Sports Med. 2011; 39(Suppl):43S–49S. [PubMed: 21709031]
9. Wassilew GI, Janz V, Heller MO, et al. Real time visualization of femoroacetabular impingement and subluxation using 320-slice computed tomography. J Orthop Res. 2013; 31(2):275–281. [PubMed: 22961635]
10. Lee CB, Clark J. Fluoroscopic demonstration of femoroacetabular impingement during hip arthroscopy. Arthroscopy. 2011; 27(7):994–1004. [PubMed: 21693351]
11. Bey MJ, Zauel R, Brock SK, Tashman S. Validation of a new model-based tracking technique for measuring three-dimensional, in vivo glenohumeral joint kinematics. J Biomech Eng. 2006; 128(4):604–609. [PubMed: 16813452]
12. Lin H, Wang S, Tsai TY, Li G, Kwon YM. In-vitro validation of a non-invasive dual fluoroscopic imaging technique for measurement of the hip kinematics. Med Eng Phys. 2013; 35(3):411–416. [PubMed: 23137670]
13. Martin DE, Greco NJ, Klatt BA, Wright VJ, Anderst WJ, Tashman S. Model-based tracking of the hip: implications for novel analyses of hip pathology. J Arthroplasty. 2011; 26(1):88–97. [PubMed: 20347253]
14. Reimann, DA.; Flynn, MJ. Automated Distortion Correction of X-ray Image Intensifier Images. Conference Record of the 1992 IEEE Nuclear Science Symposium and Medical Imaging Conference; October 25–31, 1992; Orlando, FL.
15. Tashman S, Anderst W. In-vivo measurement of dynamic joint motion using high speed biplane radiography and CT: application to canine ACL deficiency. J Biomech Eng. 2003; 125(2):238–245. [PubMed: 12751286]
16. Harris MD, Anderson AE, Henak CR, Ellis BJ, Peters CL, Weiss JA. Finite element prediction of cartilage contact stresses in normal human hips. J Orthop Res. 2012; 30(7):1133–1139. [PubMed: 22213112]
17. Winter, DA. Biomechanics and motor control of human movement. 3rd ed. Hoboken, NJ: John Wiley & Sons, Inc.; 2005.
18. Wu G, Siegler S, Allard P, et al. ISB recommendation on definitions of joint coordinate system of various joints for the reporting of human joint motion--part I: ankle, hip, and spine. International Society of Biomechanics. J Biomech. 2002; 35(4):543–548. [PubMed: 11934426]
19. Victor J, Van Doninck D, Labey L, Innocenti B, Parizel PM, Bellemans J. How precise can bony landmarks be determined on a CT scan of the knee? Knee. 2009; 16(5):358–365. [PubMed: 19195896]
20. Grood ES, Suntay WJ. A joint coordinate system for the clinical description of three-dimensional motions: application to the knee. J Biomech Eng. 1983; 105(2):136–144. [PubMed: 6865355]
21. Flegal KM, Carroll MD, Kit BK, Ogden CL. Prevalence of obesity and trends in the distribution of body mass index among US adults, 1999–2010. Jama. 2012; 307(5):491–497. [PubMed: 22253363]
22. Harris JD, Erickson BJ, Bush-Joseph CA, Nho SJ. Treatment of femoroacetabular impingement: a systematic review. Curr Rev Musculoskelet Med. 2013; 6(3):207–218. [PubMed: 23743861]

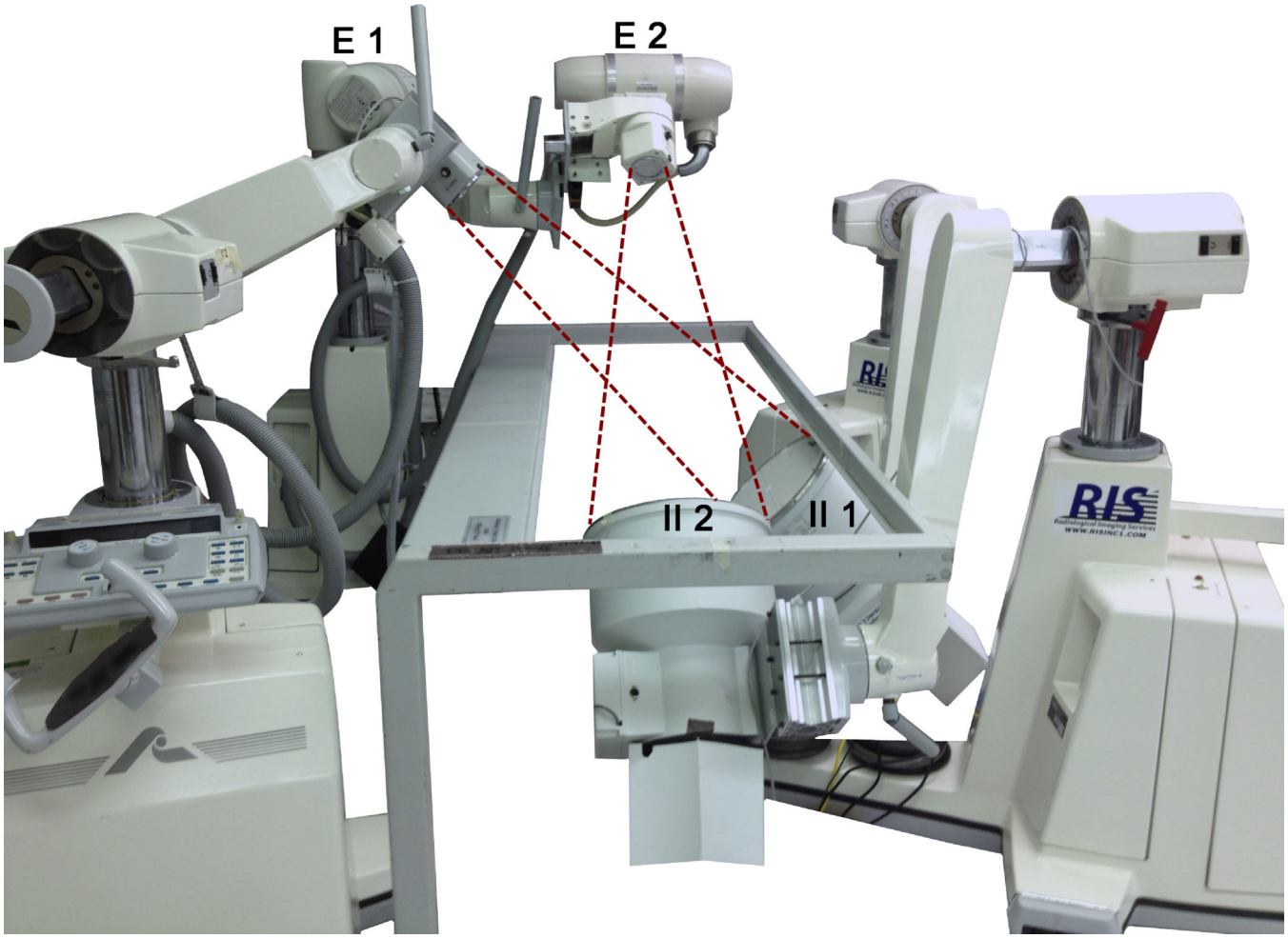

Figure 1.
Dual fluoroscopy system configured to image the left hip during supine clinical exams (E = emitter, II= image intensifier). Dashed lines represent x-ray beam.

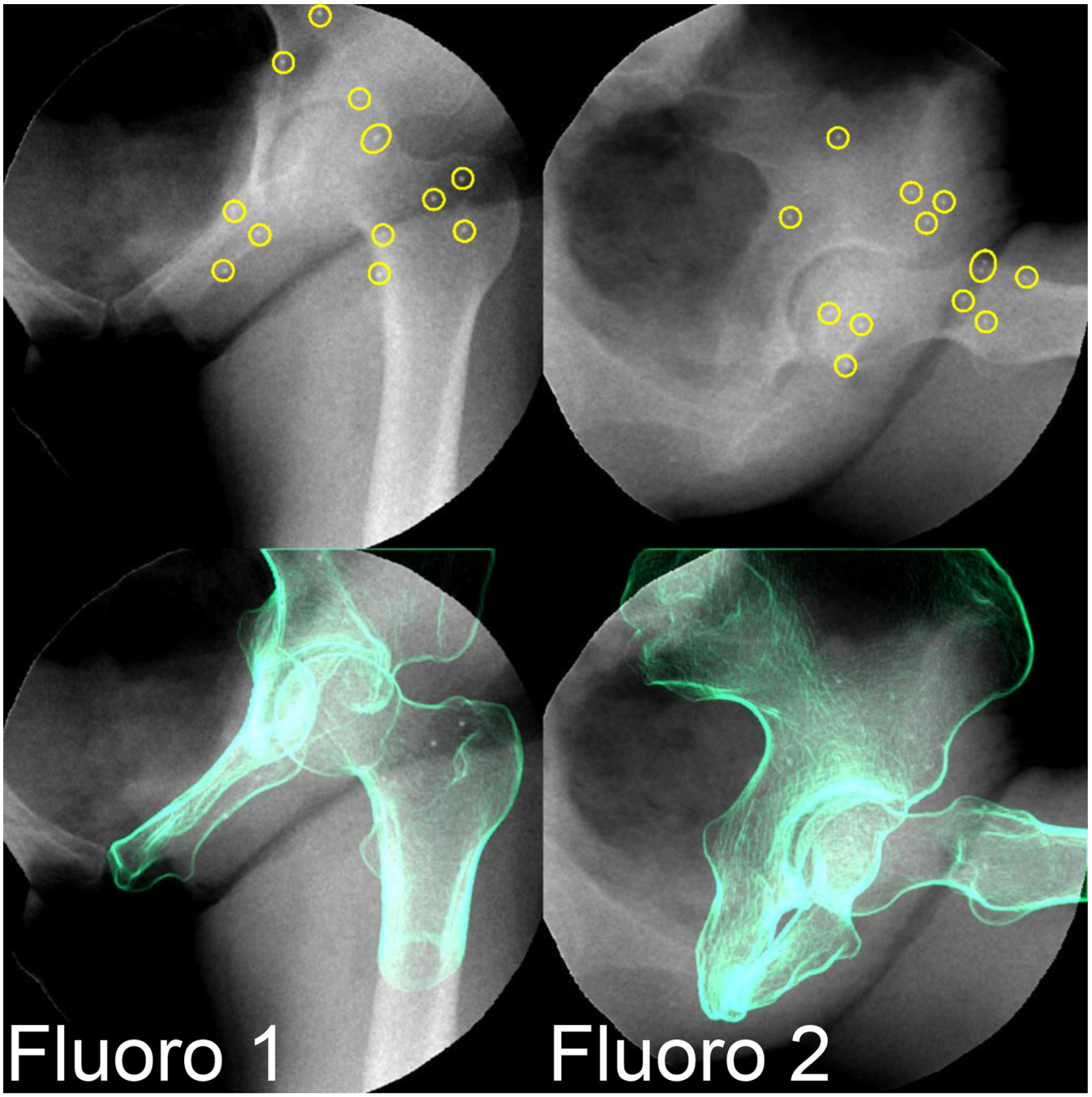

Figure 2.
Fluoroscopy images from Specimen 2 during the impingement exam. Point of max internal rotation at ~90° flexion is shown. Top: Fluoroscopy images with circles highlighting the beads implanted in pelvis and proximal femur. Bottom: Fluoroscopy images with digitally reconstructed radiographs of the pelvis and femur overlaid.

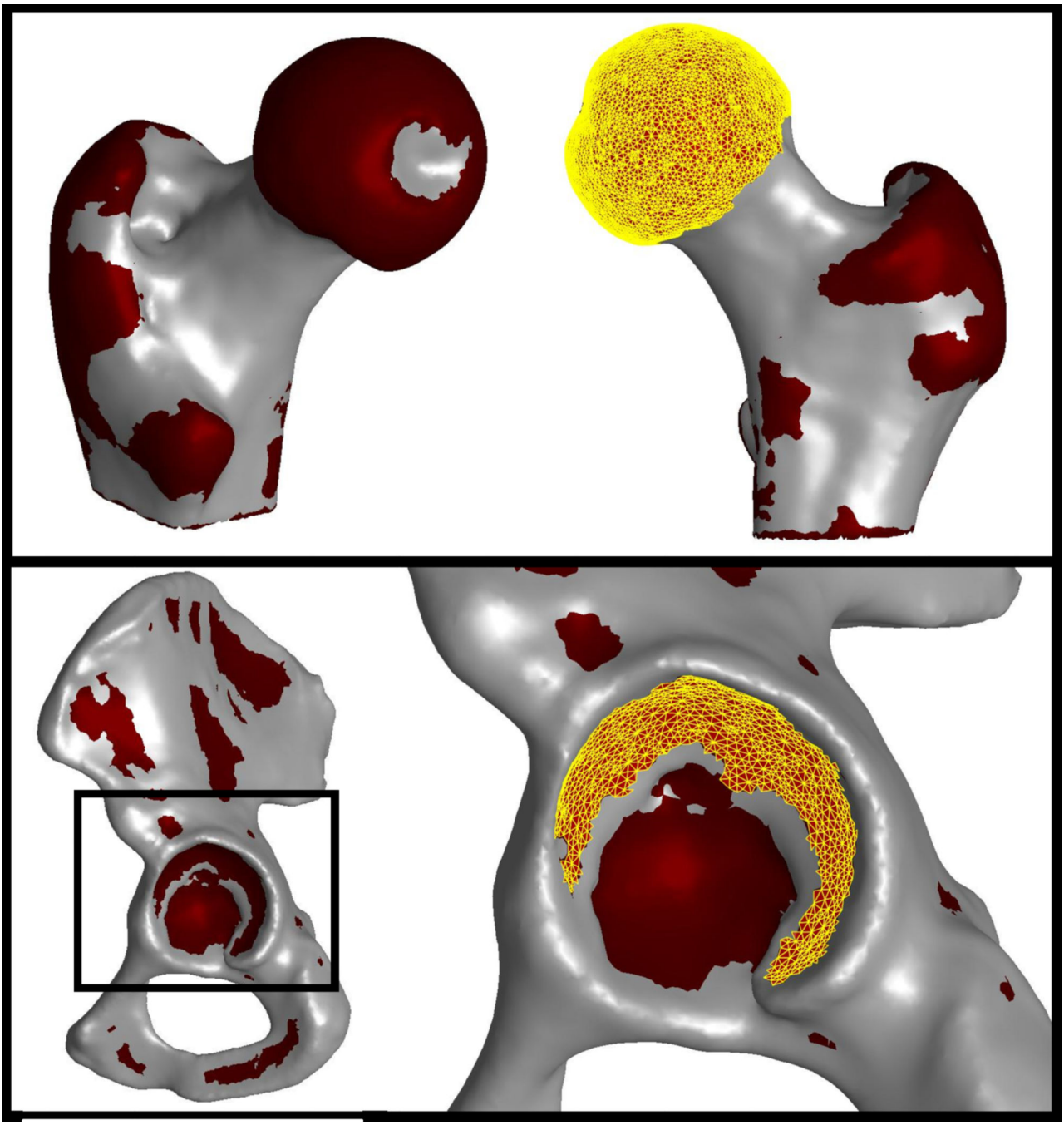

Figure 3.
Methods to find pelvic and femoral joint centers. Second principal curvature automatically isolates femoral head (top) and lunate surface of the acetabulum (bottom). The pelvic and femoral joint centers were calculated as the center of the best fit sphere of the lunate surface of the acetabulum and femoral head, respectively.

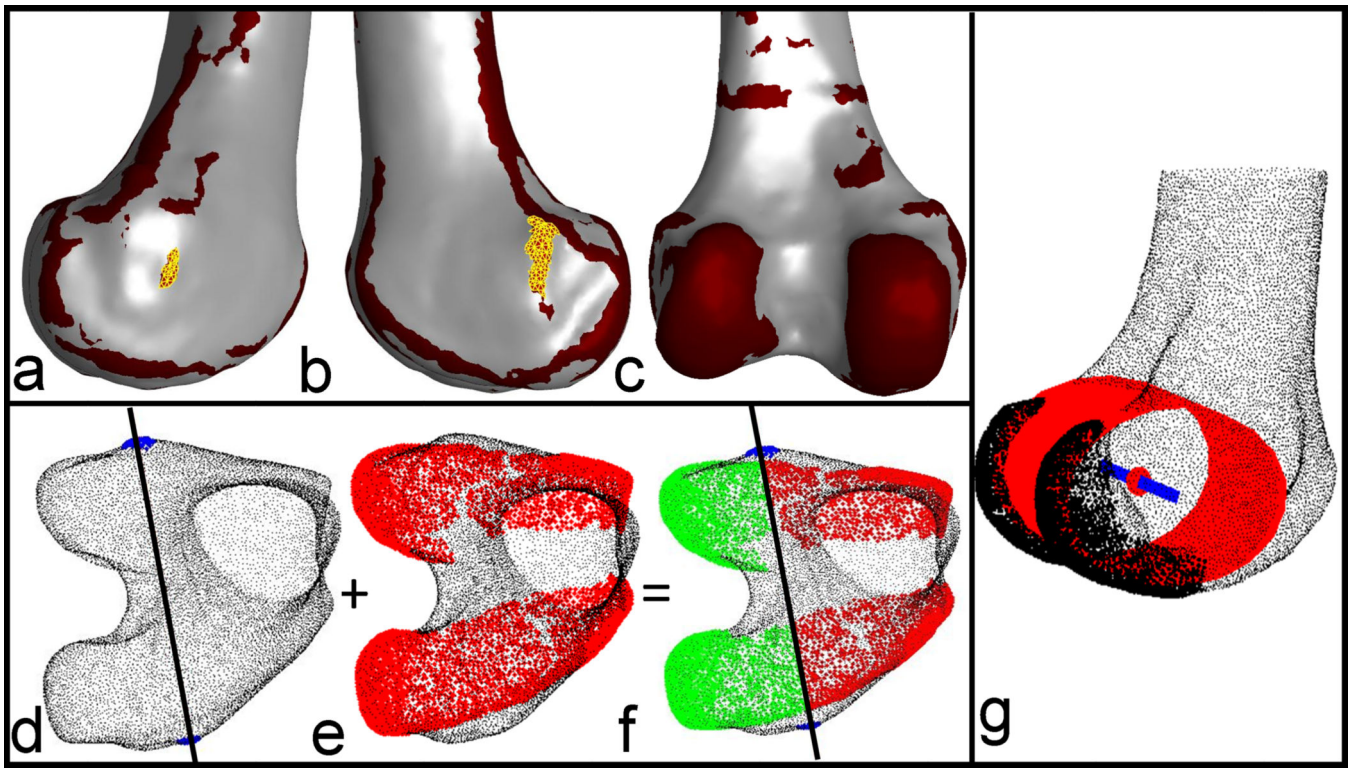

Figure 4.

Methods to establish the mediolateral axis of the femur and midpoint of the knee. First principal curvature automatically defined the ridges on the medial and lateral femoral epicondyles [yellow selection in (a), (b)]. The articulating surface of the condyles was automatically defined using second principal curvature [red selection in (c), (e)]. A plane was fit to the medial and lateral epicondyle ridges [blue in (d)] to isolate the posterior condyles [green in (f)]. The isolated posterior condyles were fit to a cylinder [red in (g)] to define the mediolateral axis of the femur [blue in (g)]. The center of the cylinder defined the midpoint (g).

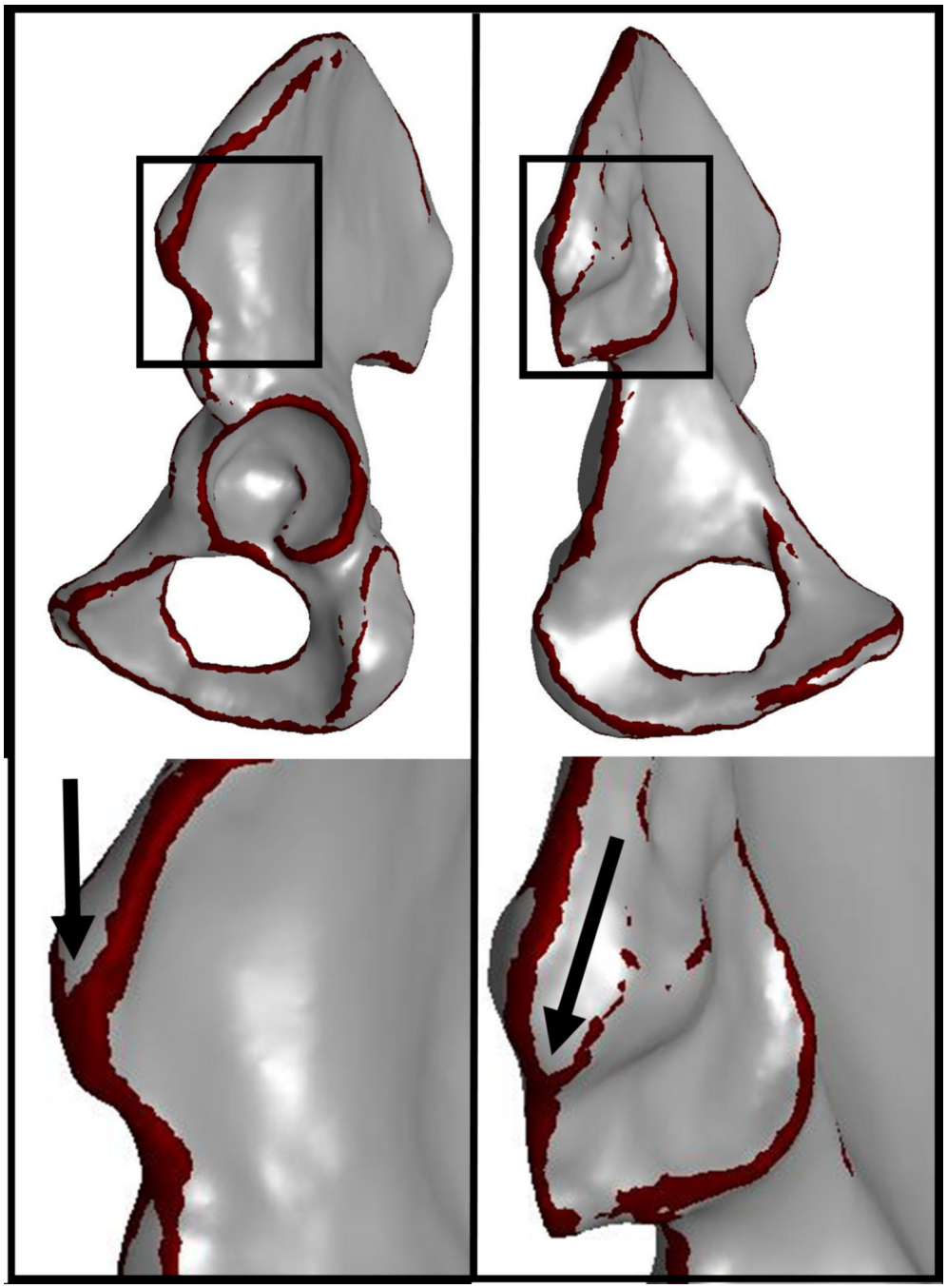

Figure 5.

Methods to identify the anterior superior iliac spines (ASIS) and posterior superior iliac spines (PSIS). First principal curvature automatically defined the iliac crest and superior border of the sacroiliac joint. The ASIS was identified as a user-selected point at the anterior intersection between the medial and lateral borders of the iliac crest (arrow, left panel). The PSIS was identified as a user-selected point at the posterior intersection of the superior border of the sacroiliac joint and the medial border of the iliac crest (arrow, right panel).

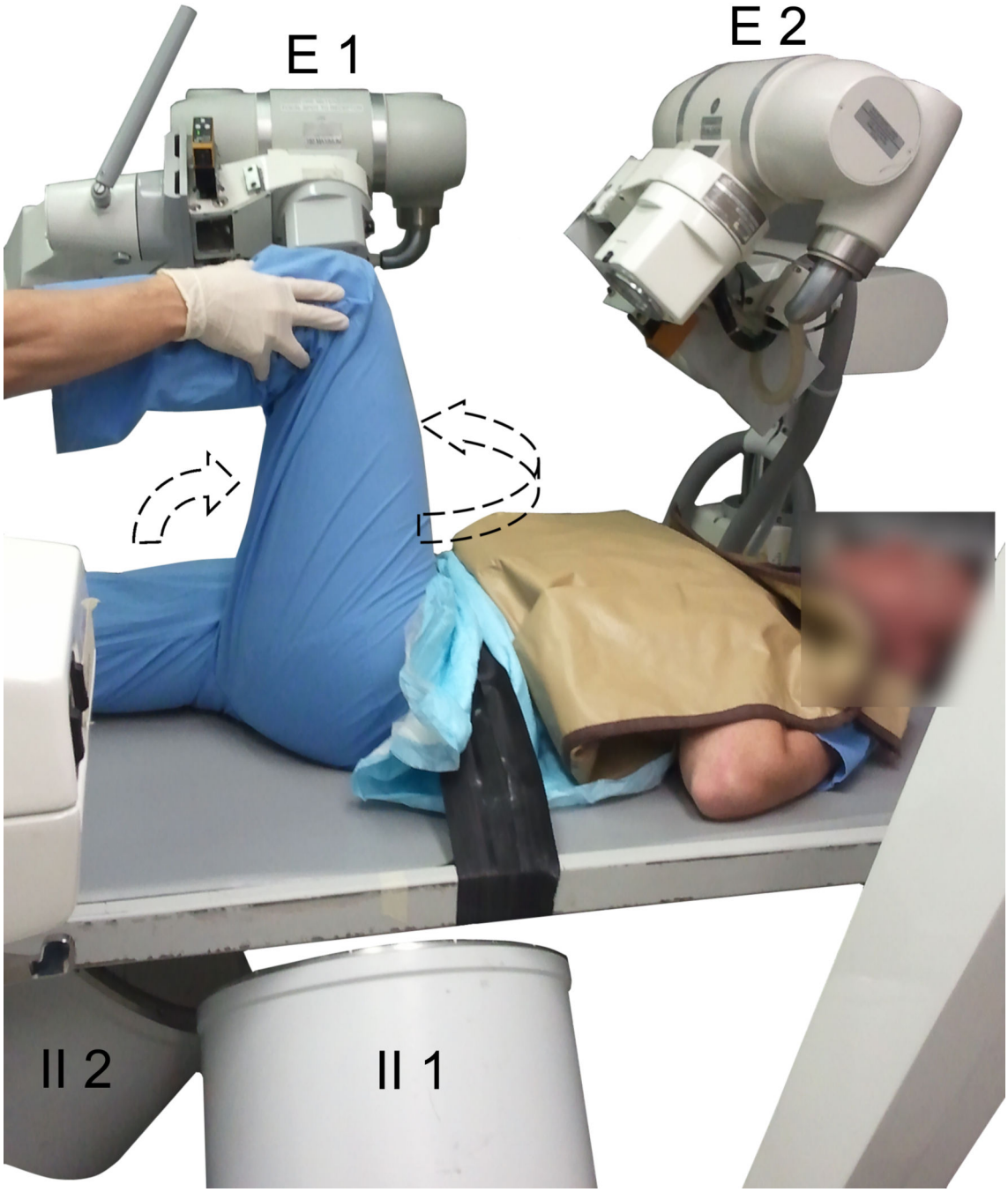

Figure 6.
Live subject positioned in the dual fluoroscopy system with left hip flexed during impingement exam. Dashed arrows indicate the direction of motion during the impingement exam, specifically flexion to ~90° followed by internal rotation and adduction.

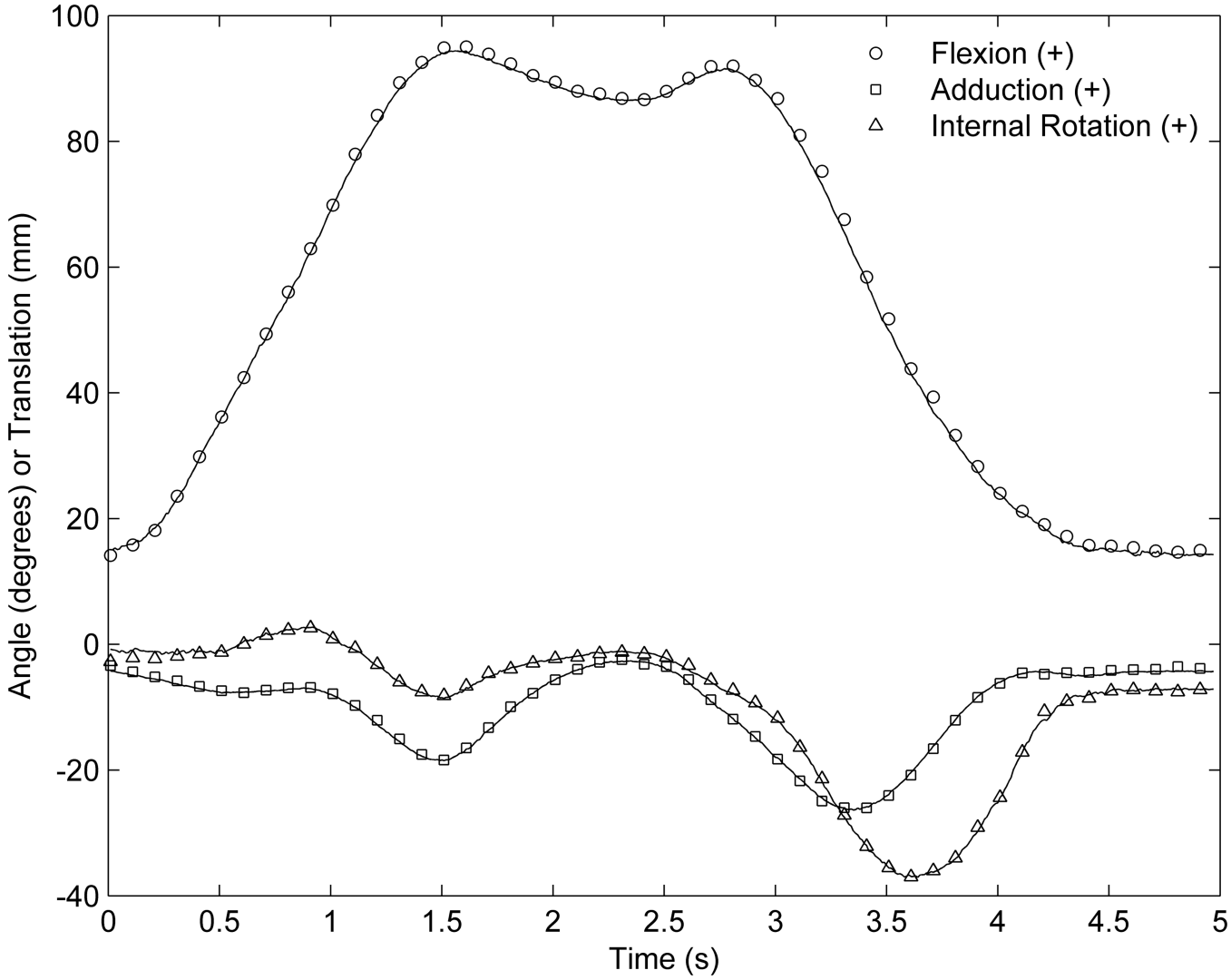

Figure 7.

Results for specimen 1 during the impingement exam. Joint angles calculated via model-based tracking (lines) are compared to DRSA (shapes, plotted every 10th frame for clarity).

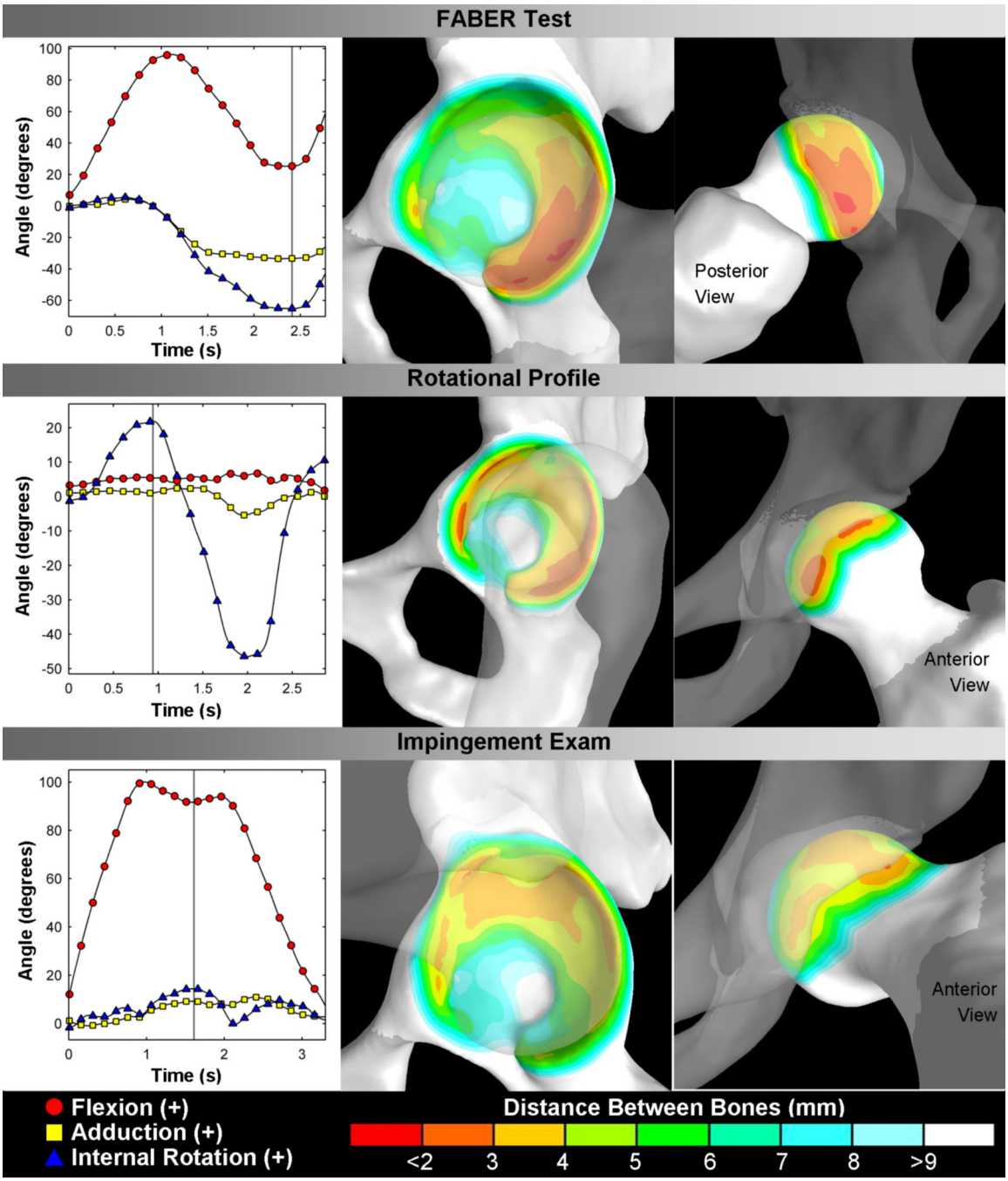

Figure 8.

Joint angles calculated using model-based tracking during clinical exams on live subject (left column). Bone-bone distance (mm) is displayed on pelvis (middle column) and femur (right column) at time points indicated in joint angle plots by vertical grey line. Included time points are: max external rotation for the FABER test, max internal rotation for the rotational profile, and max internal rotation in flexion for the impingement exam.

Table 1

Model-Based Tracking Bias and Precision of Sphere Centroid Locations

		FABER Test		Impingement Exam		Rotational Profile	
		Bias	**Precision**	**Bias**	**Precision**	**Bias**	**Precision**
Pelvis	3D	0.35 (0.09)	0.15 (0.03)	0.35 (0.07)	0.14 (0.03)	0.26 (0.07)	0.11 (0.03)
	X	−0.14 (0.10)	0.14 (0.04)	−0.16 (0.13)	0.16 (0.04)	−0.06 (0.06)	0.14 (0.05)
	Y	0.03 (0.04)	0.09 (0.02)	0.04 (0.05)	0.09 (0.02)	0.07 (0.07)	0.08 (0.03)
	Z	0.12 (0.23)	0.17 (0.04)	0.09 (0.18)	0.17 (0.03)	0.06 (0.12)	0.15 (0.05)
Femur	3D	0.30 (0.06)	0.15 (0.04)	0.26 (0.05)	0.13 (0.05)	0.34 (0.07)	0.14 (0.03)
	X	0.07 (0.06)	0.13 (0.02)	0.11 (0.07)	0.11 (0.03)	0.03 (0.13)	0.13 (0.03)
	Y	−0.05 (0.09)	0.13 (0.04)	0.01 (0.05)	0.10 (0.02)	0.03 (0.06)	0.13 (0.03)
	Z	−0.04 (0.09)	0.23 (0.04)	0.04 (0.12)	0.17 (0.05)	0.17 (0.08)	0.21 (0.04)

All results in mm. Results are listed at average (standard deviation) for three beads tracked in two specimens for three trials per exam. 3D represents Euclidian distance between sphere centroids. X, Y, Z represent the difference along each of the laboratory axes.

Table 2

Model-based Tracking Bias and Precision of Joint Angles and Translations

	FABER Test		Impingement Exam		Rotational Profile	
	Bias	**Precision**	**Bias**	**Precision**	**Bias**	**Precision**
Mediolateral (mm)	0.35 (0.10)	0.32 (0.10)	0.36 (0.26)	0.48 (0.65)	0.23 (0.28)	0.42 (0.05)
Anteroposterior (mm)	0.10 (0.27)	0.41 (0.11)	0.06 (0.31)	0.38 (0.07)	−0.22 (0.22)	0.51 (0.16)
Superoinferior (mm)	0.27 (0.20)	0.47 (0.15)	0.48 (0.65)	0.59 (0.22)	0.03 (0.21)	0.25 (0.04)
Flex-Extension (°)	0.28 (0.22)	0.78 (0.31)	0.26 (0.44)	0.54 (0.08)	0.49 (0.16)	0.57 (0.14)
Ab-Adduction (°)	0.03 (0.32)	0.36 (0.12)	−0.06 (0.29)	0.44 (0.13)	0.55 (0.18)	0.38 (0.06)
Int-Ext Rotation (°)	−0.14 (0.20)	0.71 (0.13)	−0.58 (0.66)	0.74 (0.23)	−0.21 (0.57)	0.76 (0.20)

Results are listed at average (standard deviation) of three trials for each exam completed for two specimens.

Table 3

Maximum bias and precision comparison between studies

Maximum Reported Value	Present Study	Martin et al., 2011	Lin et al., 2012
Bias along a single laboratory axis (mm)	0.17	0.21	*
Precision along a single laboratory axis (mm)	0.21	0.24	*
Joint Angle Bias (°)	0.58	0.43	0.59
Joint Angle Precision (°)	0.78	1.27	0.82
Translation Bias (mm)	0.48	0.4	0.93
Translation Precision (mm)	0.59	0.45	1.13

* Lin et al. reported error along anatomical axes, not laboratory axes.